nature catalysis

ARTICLES

https://doi.org/10.1038/s41929-018-0168-4

Copper nanocavities confine intermediates for efficient electrosynthesis of C3 alcohol fuels from carbon monoxide

Tao-Tao Zhuang[1,9], Yuanjie Pang[1,2,3,9], Zhi-Qin Liang[1], Ziyun Wang[1], Yi Li[4], Chih-Shan Tan[1], Jun Li[1,2], Cao Thang Dinh[1], Phil De Luna[5], Pei-Lun Hsieh[6], Thomas Burdyny[2], Hui-Hui Li[1,4], Mengxia Liu[1], Yuhang Wang[1], Fengwang Li[1], Andrew Proppe[1,7], Andrew Johnston[1], Dae-Hyun Nam[1], Zhen-Yu Wu[4], Ya-Rong Zheng[4], Alexander H. Ip[1], Hairen Tan[1], Lih-Juann Chen[6], Shu-Hong Yu[4], Shana O. Kelley[7,8], David Sinton[2]* and Edward H. Sargent[1]*

The electrosynthesis of higher-order alcohols from carbon dioxide and carbon monoxide addresses the need for the long-term storage of renewable electricity; unfortunately, the present-day performance remains below what is needed for practical applications. Here we report a catalyst design strategy that promotes C3 formation via the nanoconfinement of C2 intermediates, and thereby promotes C2:C1 coupling inside a reactive nanocavity. We first employed finite-element method simulations to assess the potential for the retention and binding of C2 intermediates as a function of cavity structure. We then developed a method of synthesizing open Cu nanocavity structures with a tunable geometry via the electroreduction of Cu_2O cavities formed through acidic etching. The nanocavities showed a morphology-driven shift in selectivity from C2 to C3 products during the carbon monoxide electroreduction, to reach a propanol Faradaic efficiency of 21 ± 1% at a conversion rate of 7.8 ± 0.5 mA cm^{-2} at −0.56 V versus a reversible hydrogen electrode.

The electrocatalytic reduction of CO_2 to valuable carbon-based chemical feedstocks offers a route to the long-term storage of renewable electricity that closes the carbon cycle[1–8]. The higher-order alcohol *n*-propanol is desired for its high volumetric energy density (27 MJ l^{-1}) (ref. [9])—cost-effective renewable propanol would offer a sustainable liquid fuel for existing internal combustion engines.

It is of interest, therefore, to explore means of increasing selectivity in favour of electrochemical propanol production[10–12]. With CO_2-to-CO conversion now well established[13,14], a subsequent electrocatalytic CO-to-propanol conversion shows promise[15–17]; however, even here selectivities remain in the vicinity of 10% (refs [18,19]), primarily owing to the preferred selectivity for C2 products.

Given that C3 formation can proceed via C–C coupling between C2 and C1 intermediates[20], we hypothesized that modifying catalysts to target C2 intermediate binding could potentially be used to promote C3 production.

We used finite-element method (FEM) simulations to study how a nanocavity confinement structure affects the binding and retention of C2 intermediates. This, we found, suppresses the net C2 loss that otherwise curtails C3 production. We then implemented three-dimensional (3D) nanocavity Cu catalysts employing an in situ electroreduction strategy, starting from Cu_2O nanoparticles (precatalyst) that exhibited an open structure.

Prior studies of porous catalysts exploited confined intermediates to some degree. One study used the confinement effect to explain a selectivity shift from C1 to C2 (ref. [21]). Here we further apply the confinement effect to boost C3 production by extending the retention of C2 species, and we provide a comprehensive model that tracks the key species. The clearly mapped confinement model guides the design of catalysts, and enables a shift in selectivity away from C2 products that leads to higher C3 production. The optimal nanocavity catalyst reduces CO to propanol with a 21 ± 1% Faradaic efficiency at a conversion rate of 7.8 ± 0.5 mA cm^{-2} at −0.56 V versus a reversible hydrogen electrode (RHE).

Results

FEM simulations. We hypothesized that a nanocavity structure could potentially concentrate C2 species via steric confinement and thereby limit the desorption of C2 intermediates and promote further conversion into a C3 product. We used FEM simulations to explore the prospects of cavity-enhanced C3 selectivity. Hollow spherical shells[21–23] (with an outer diameter of 100 nm and an inner diameter of 60 nm) with circular openings of various central angles were used to represent nanocavities immersed in an aqueous electrolyte (Supplementary Fig. 1a). In these simulations, CO molecules diffused to the surface (Fig. 1a and Supplementary Fig. 1b) and then were adsorbed and converted into C2 species at both the interior

[1]Department of Electrical and Computer Engineering, University of Toronto, Toronto, Ontario, Canada. [2]Department of Mechanical and Industrial Engineering, University of Toronto, Toronto, Ontario, Canada. [3]School of Optical and Electronic Information, Huazhong University of Science and Technology, Wuhan, Hubei, China. [4]Division of Nanomaterials & Chemistry, Hefei National Laboratory for Physical Sciences at Microscale, Collaborative Innovation Center of Suzhou Nano Science and Technology, CAS Center for Excellence in Nanoscience, Department of Chemistry, University of Science and Technology of China, Hefei, Anhui, China. [5]Department of Materials Science and Engineering, University of Toronto, Toronto, Ontario, Canada. [6]Department of Materials Science and Engineering, National Tsing Hua University, Hsinchu, Taiwan. [7]Department of Chemistry, University of Toronto, Toronto, Ontario, Canada. [8]Department of Pharmaceutical Sciences, Leslie Dan Faculty of Pharmacy, University of Toronto, Toronto, Ontario, Canada. [9]These authors contributed equally: Tao-Tao Zhuang and Yuanjie Pang. *e-mail: sinton@mie.utoronto.ca; ted.sargent@utoronto.ca

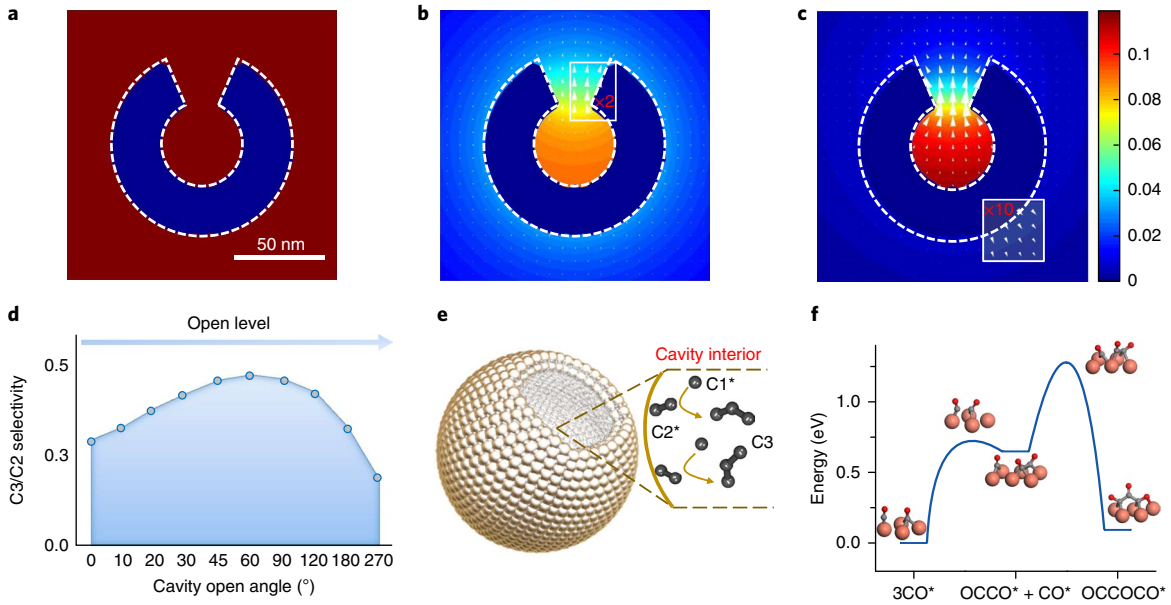

Fig. 1 | Computed concentration and flux distribution of species. a–c, CO (**a**), C2 (**b**) and C3 (**c**) concentrations (colour scale, in millimoles) and flux distributions (arrows) on the cavity confinement structure. **d**, Ratio of C3/C2 productivity, measured by the total outflux of C2 and C3 products, as a function of cavity open angle. **e**, The schematic shows how the cavity confinement effect promotes C2 species binding and further conversion to C3. *The surface species. **f**, Energy profile of the C3 formation intermediate. The geometries of intermediate states and transition states are shown as insets (only the CO species in the reaction are illustrated). Red, oxygen; grey, carbon; orange, copper.

and exterior surfaces of the nanoparticle (Fig. 1b and Supplementary Fig. 1c). The C2 species may then either desorb from the reactive surface as a C2 product, or be coupled with a CO molecule to form a C3 product (Fig. 1c and Supplementary Fig. 1d,e). We found that the cavity restricts the outflow of locally produced C2 species (Fig. 1b, arrows), which leads to higher local C2 intermediate concentrations inside the cavity (Fig. 1b, colour map). The desorption of C2 intermediates is then reduced, which leads to an increased surface coverage and residence of the intermediates necessary for C3 production, and ultimately generates a heightened C3 production rate inside the cavity (Fig. 1c).

In contrast, solid nanoparticles are not predicted to restrict materially the transport of C2 reactants away from their surfaces, which leads to lower C2:C1 coupling rates (Supplementary Fig. 2a). To study the bounds of the cavity-enhancement effect, we quantitatively assessed the angular dependence of the nanocavity on C2 versus C3 selectivity from fully closed to fully open structures (Supplementary Fig. 2). Specifically, we monitored the outflux of C2 and C3 products from both the interior and exterior surfaces of the structures (Supplementary Fig. 3a). The productivity of both species in the interior cavity of the particles showed a strong dependence on the opening angle, in strong contrast to that at the exterior surfaces (Supplementary Fig. 3b–d). At small opening angles (<30°), C2 and C3 productivities are low as the CO reagent transport into the cavity is unduly restricted, which results in CO limitation. At large opening angles (>180°), the cavity does not succeed in containing the generated C2, and exhibits a lower C3/C2 selectivity than all the other cases. At intermediate angles (45–90°), the C3/C2 selectivity and overall C3 productivity appreciably exceed those found in the comparison cases (Fig. 1d and Supplementary Table 1), with a maximum at ~60°. The interior and exterior in these cases produce a similar amount of total C2+species (the sum of C2 and C3)—it is the ratio of C3 to C2 that is appreciably higher for the cavity interior. In these cases, the enrichment of C2 is not restricted by the reduced CO influx, which results in an approximate 2.8-fold enhancement

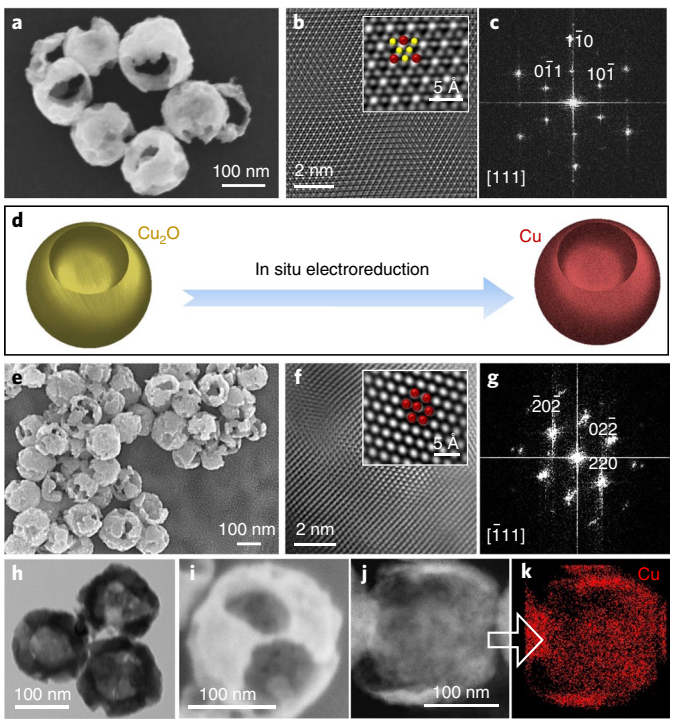

Fig. 2 | Structural characterization of the 3D cavity confinement in nanocatalysts. a–c, The cavity structures in the particles of the initial Cu_2O nanomaterial shown by SEM (**a**), STEM-ADF (magnified in the inset) (**b**) and a corresponding FFT image (**c**). **d**, The fabrication of the cavity Cu nanocatalyst via the in situ electroreduction from the initial Cu_2O. **e–k**, The SEM (**e**, **i**), STEM-ADF (**f**), FFT (**g**), TEM (**h**), STEM (**j**), and EDS (**k**) mapping images for the derived Cu show the retaining cavity structure. Cu, red; O, yellow.

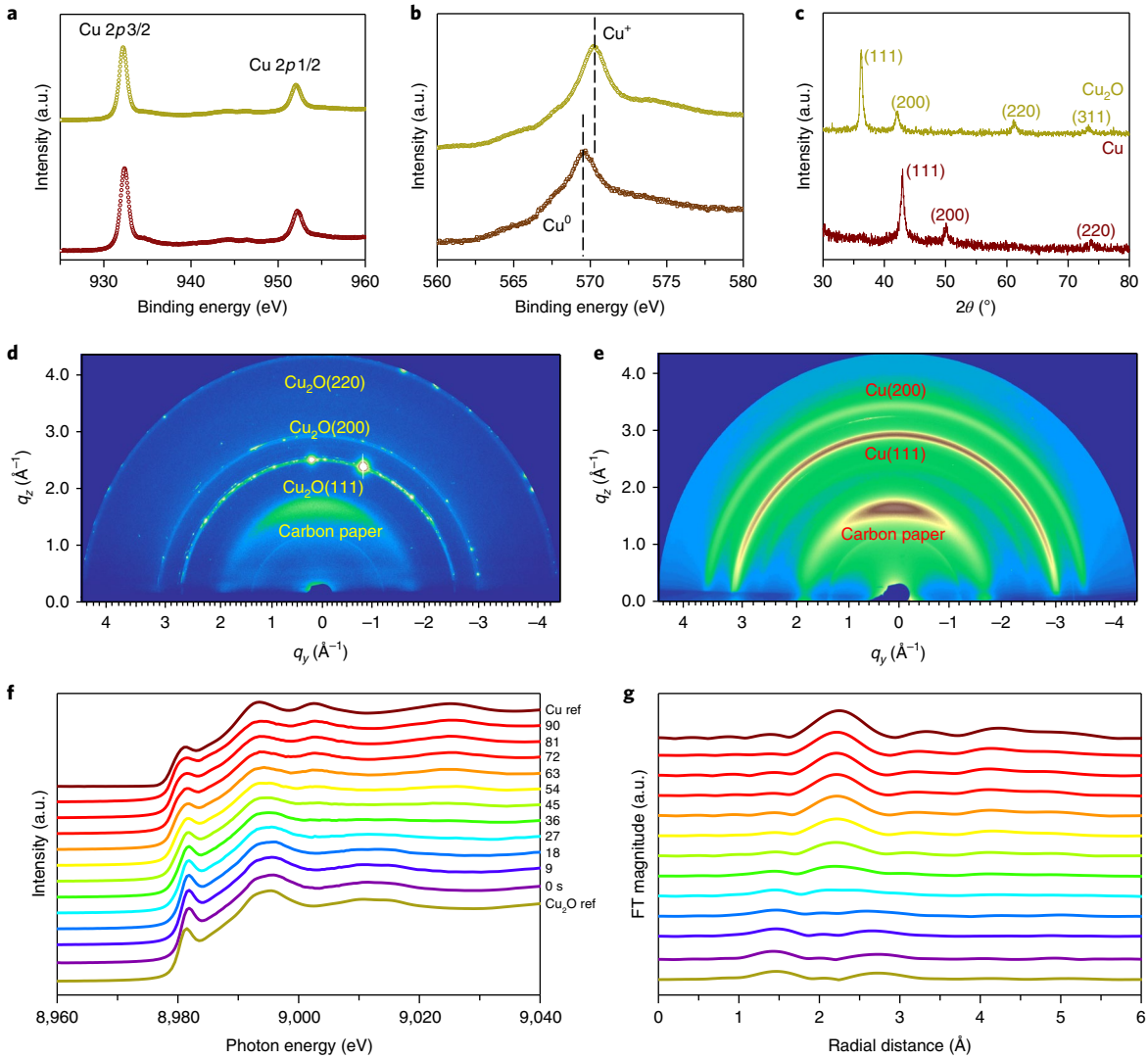

Fig. 3 | Characterization of the as-prepared Cu_2O and post-CORR Cu nanocatalysts. a, **b**, The X-ray photoelectron spectra of Cu 2*p* (**a**) and Cu LMM (**b**) of the as-prepared Cu_2O (yellow) and post-CORR Cu (red) nanocatalysts synthesized via in situ electroreduction show the change from Cu^+ to Cu^0. **c**–**e**, The powder X-ray diffraction spectra (**c**) and grazing incidence wide-angle X-ray scattering 2D maps of the nanocavity electrodes show the material phase change from Cu_2O (**d**) to Cu (**e**). **f**,**g**, The in situ X-ray absorption spectral measurements of the Cu_2O nanocavity electrode with time evolution (0–90 s) in a flow cell system further verify the pure Cu in a 3D nanocavity electrode after electroreduction. **f**, In situ Cu K edge X-ray absorption near-edge spectra. **g**, Extended X-ray absorption fine structure. Ex situ Cu K edge X-ray absorption spectroscopy of Cu_2O and metallic Cu were performed as standards. a.u., arbitrary units. FT, Fourier transform; ref, reference.

of C3/C2 production for this optimized cavity opening. Altogether, these simulations point to a nanocavity intermediate confinement as a promising means to enhance the production of higher carbon products (Fig. 1e).

We also calculated the formation of C3 on Cu(111) using density functional theory (DFT) including C1:C1 and C1:C2 coupling steps[20]. C2 formation is first calculated based on the dimerization of CO (Fig. 1f, Supplementary Fig. 4 and Supplementary Table 2)[19]. In CO reduction, CO is abundant on the surface owing to the strong adsorption energy of CO compared to that of CO_2; thus, the C2 and CO coupling was assumed to be one of the most likely pathways for C3 formation (Fig. 1f, Supplementary Fig. 5 and Supplementary Table 2). Our calculations suggest that the coupling of C2 with a CO is favourable both thermodynamically and kinetically. The findings also suggest that the low stability of the C2 species will lead to a low C2 surface coverage, a fact that reduces the likelihood that CO and C2 will meet to form C3; this accounts for the need to concentrate the C2 species via the nanocavity strategy.

Catalyst preparation and characterization. We sought, therefore, to fabricate a tunable nanocavity copper catalyst. We first synthesized Cu_2O nanoparticles (with average sizes of 110 ± 20 nm, comparable to the scale of simulations) via the nucleation and growth of nanocrystals[24]. By applying a gentle acidic etching technique, we then produced open structures, controlling the size of the hole via exposure time[25] (details in Methods). We characterized the resulting Cu_2O particles using scanning electron microscopy (SEM), and witnessed an open morphology in the majority of nanoparticles (Fig. 2a). We further characterized the particles via scanning transmission electron microscopy annular dark field (STEM-ADF), the corresponding fast Fourier transform (FFT) and energy-dispersive X-ray spectroscopy (EDS) mapping (Fig. 2b,c and Supplementary Fig. 6a).

After the synthesis, we deposited the Cu_2O particles onto a carbon substrate, and then produced the final nanocavity Cu catalyst (Fig. 2d) via an in situ CO electrochemical reduction. SEM and TEM images confirmed that the catalyst produced after the CO

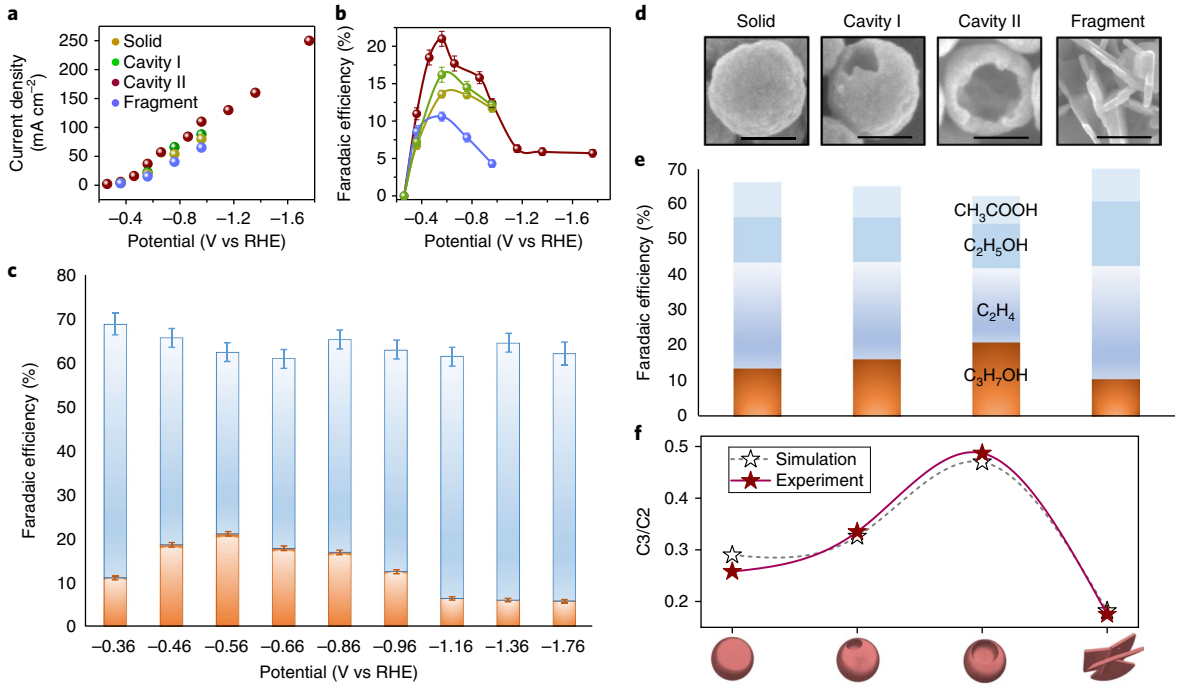

Fig. 4 | CO electrochemical reduction performance in a flow cell system. a, Plot of current density versus applied potential on Cu-based catalysts with the morphology structures of solid, cavity I, cavity II and fragment. **b**, Propanol Faradaic efficiencies on the catalysts at different applied potentials show that the cavity II catalyst has the best selectivity of these structures. **c**, Faradaic efficiencies of C2 products (acetate, ethanol and ethylene) (blue) and C3 propanol (orange) on the cavity II Cu catalyst under a range of applied potentials. **d**, Representative SEM images of these catalysts. Scale bars, 100 nm. **e**, Faradaic efficiencies of C2 and C3 products on these catalyst morphologies (**d**) at the applied potential of −0.56 V versus RHE. **f**, The experimental and FEM simulation results of the C3/C2 product selectivity on different catalysts show a good agreement. Error bars in **a**–**c** correspond to the s.d. of three or more measurements.

reduction reaction (CORR) retained the particle size and the open morphology of the original Cu_2O, whereas the material structure had been electrochemically reduced to pure Cu, as demonstrated by STEM-ADF, FFT, TEM, STEM and EDS mapping (Fig. 2e–k and Supplementary Figs. 6b,c and 7).

To characterize the in situ electroreduced electrodes and gain an insight into the chemical state of the active catalyst, a series of spectral measurements were made on the as-prepared and electrochemically derived samples. The spectra of Cu 2*p* and Auger Cu LMM conducted by X-ray photoelectron spectroscopy, taken together, show the valence state transition from Cu^+ to Cu^0 (Fig. 3a,b). We used powder X-ray diffraction and grazing incidence wide-angle X-ray scattering to confirm the phase change from cuprite Cu_2O to cubic Cu (Fig. 3c–e).

The Cu K edge X-ray absorption near-edge spectra and the extended X-ray absorption fine structure of the catalyst and corresponding reference standard materials demonstrated that the Cu_2O was reduced to Cu in less than 100 seconds after the reaction, which reconfirms that the final nanocavity catalyst is metallic Cu (Fig. 3f,g).

Taken together, these studies (Figs. 2 and 3 and Supplementary Fig. 8) indicate that this feature of the Cu nanocavity catalyst is, regardless of other established factors, known to influence the electroreduction performance, such as oxidation state[26], Cu defects[27], oxygen doping[28] or grain boundary density[29], as documented in prior studies.

Electrochemical CO reduction performance. We then explored the CORR activity of the Cu catalysts derived from the solid, cavity I, cavity II and fragment morphologies (Fig. 4d and Supplementary Fig. 9). We deposited the catalyst onto a carbon gas-diffusion electrode via spray coating of a material ink (Methods) and tested the samples in an engineered flow-cell configuration (Supplementary Fig. 10). Compared to conventional hydrogen cells, the flow cells with gas-diffusion electrodes increased the gas reactant availability at the electrode surface[30].

The current density recorded on the cavity II sample was larger than those of other opening angles at the same applied potential (Fig. 4a). Once normalized by the electrochemical surface area (Supplementary Fig. 11a–i), the current densities presented similar values (Supplementary Fig. 11j,k) across samples and across the potential range applied. We concluded that the overall activity towards the CORR is substantially independent of the cavity morphology, and thus turned our attention to the selectivity.

We evaluated the electrocatalytic CO reduction performance in the potential range of −0.36 V to −1.76 V versus the RHE in 1 M KOH solution. Propanol was detected using ^{1}H NMR spectroscopy. The cavity II nanocatalyst showed the highest Faradaic efficiency of propanol compared to the other samples over the entire potential range, which demonstrates the structural effect of cavity confinement on the propanol selectivity. As Cu is an electrical conductor, the cavity structures are not expected to introduce a difference in the electric potential over the entire surface (including the interior and the exterior) of the cavity (Supplementary Fig. 12 gives the modelling result). At −0.56 V versus RHE, the Faradaic efficiency for propanol in the cavity II sample reaches 21 ± 1% (Fig. 4b) with a partial current density of 7.8 ± 0.5 mA cm^{-2} (Supplementary Table 3). We compare in Supplementary Table 4 this performance with that of catalysts previously reported in the published literature.

The carbon-based product distribution, obtained using NMR spectroscopy (Supplementary Fig. 13a) and gas chromatography, which included C2 (acetate, ethanol and ethylene) and

propanol from the cavity II nanocatalyst, is shown in Fig. 4c. Supplementary Table 5 compares cavity II with the solid, cavity I and fragment controls.

The nanoconfinement of carbon-based intermediates within the cavity structures of Cu catalysts (Fig. 4d) enabled a shift of product selectivity to C3 propanol. The combined product distributions at the optimized applied potential of −0.56 V versus RHE (Fig. 4e) show that the increased propanol production in the cavity II structure corresponds to a decreased ethylene formation, with the mix of acetic acid and ethanol remaining similar to that of the other catalyst structures. These results indicate that the C2 intermediate for propanol production via C–C coupling with CO inside the cavity is related to the ethylene, in agreement with previously reported mechanisms for propanol production[11,31], and as modelled in the FEM simulations here. We examined the performance and structure change of the catalyst with time evolution (Supplementary Figs. 13b,c and 14). After two hours of testing, the catalyst reconstructed to form aggregated Cu particles (Supplementary Fig. 14d–f) that decreased the Faradaic efficiency of propanol from 21% to 14% and shifted the selectivity from C3 to C2 products (Supplementary Fig. 13c). This result further confirms the nanocavity scenario as the source of the high C3 content.

We compared the experimental and simulated ratio of C3/C2 products. The FEM model qualitatively agrees with the experimental data in terms of the best geometry for C3 production, regardless of the adsorption/desorption equilibrium constants and reaction rate constants used in the model (Supplementary Figs. 15–18). The FEM results can be further fitted to the experimental data to obtain qualitative agreements between the two (Fig. 4f) and the resulting parameters follow the trend predicted by the DFT calculations. This relatively simple model captures the key transport and geometric aspects of the nanocavities and provides a physical picture of the diffusive trapping of C2 intermediates and the resulting enhancement in C3 production.

Conclusions

This work provides a catalyst structuring approach wherein the desired intermediates are concentrated to direct selectivity along a desired reaction pathway. FEM simulations, material structure characterization and electrochemical measurements attest to the role of the nanocavity catalyst in improving the catalytic performance and directing electrons to higher carbon products. These findings provide a physical route to tuning chemical selectivity and enabling the electroproduction of renewable liquid fuels and feedstocks.

Methods

FEM simulations. FEM simulations were performed using the COMSOL Multiphysics software package (https://www.comsol.com/). Three modules were used to establish a comprehensive chemistry–mass transport model of the nanocavity structure[32–34]. Supplementary Methods gives detailed information regarding the FEM simulations.

DFT calculations. In this work, all the DFT calculations were carried out with a periodic slab model using the Vienna ab initio simulation program (VASP) (https://www.vasp.at/). Supplementary Methods gives detailed theoretical methods.

Initial Cu_2O nanoparticles synthesis. We synthesized Cu_2O nanoparticles, which included the solid, cavity I, cavity II and fragment morphologies, according to a previously reported method[24]. In a typical procedure, 4.5 g of sodium dodecyl sulfate was dissolved in 450 ml of distilled water in a glass reactor, and then 65 mg of $CuCl_2$ added. After that, 22.5 ml of a hydroxylamine hydrochloride (310 mg) solution and 4.5 ml of a 2 M HCl solution were injected into the reactor. Next, 12.5 ml of a NaOH (500 mg) solution was quickly added into the solution. We aged the solution at room temperature for 3 h to prepare the cavity I morphology, 5 h to prepare the cavity II morphology and 9 h with 6 ml of HCl to prepare the fragment morphology. The solid Cu_2O was synthesized from the above procedure but without adding HCl and by ageing for 3 h.

Derived Cu nanocatalyst synthesis. We prepared the derived Cu nanocatalyst electrode with different morphologies via in situ CO electroreduction from the corresponding initial Cu_2O electrode, and they were obtained after an initial running (2–5 min).

Electrochemical measurements. Electrocatalytic measurements were carried out in a three-electrode system using an electrochemical station (AUT50517). All the potentials were measured against an Ag/AgCl reference electrode (3 M KCl, BASi) and converted to the RHE reference scale using:

$$E(\text{versus RHE}) = E(\text{versus Ag/AgCl}) + 0.197\ \text{V} + 0.0591 \times \text{pH} \quad (1)$$

CO reduction product analysis. Gas-phase and liquid-phase products were quantified by gas chromatography and NMR spectroscopy, respectively.

The gas chromatography, running argon (Linde, 99.999%) as a carrier gas, contained a molecular sieve 5 A and Carboxen-1000 columns. A thermal conductivity detector was used to quantify hydrogen and a flame ionization detector was used to quantify ethylene.

The liquid products were quantified using NMR spectroscopy. ^{1}H NMR spectra of freshly acquired samples were collected on an Agilent DD2 500 spectrometer in 10% D_2O using a water suppression mode, with dimethyl sulfoxide as an internal standard. A relaxation time of 16 s between the pulses was used to allow for complete proton relaxation. The Faradaic efficiency of the liquid products was calculated from the total amount of charge Q (coulombs) passed through the sample and the total amount of the liquid products produced n (moles). $Q = I \times t$, where I (amperes) is the reduction current at a specific applied potential and t (s) is the time for the constant reduction current.

The Faradaic efficiency (FE) of the liquid products can be calculated as:

$$\text{FE}_{\text{PrOH}} = 12 \times F \times \frac{n_{\text{PrOH}}}{Q} = 12 \times F \times \frac{n_{\text{PrOH}}}{(I \times t)} \quad (2)$$

where F is the Faraday constant.

Working electrode preparation and CO reduction measurements. To prepare a catalyst coated in a flow cell system, we deposited 10 mg of catalyst mixed with 20 µl of 5 wt% Nafion in 1 ml of methanol on a carbon gas-diffusion layer, ~1 mg cm^{-2}, using an airbrush. We combined the diffusion-layer-coated catalyst, anion exchange membrane and nickel anode together using polytetrafluoroethylene spacers such that a liquid electrolyte could be introduced into the chambers between the anode and membrane as well as the membrane and the cathode. Gaseous CO was passed through the gas chamber at the back side of the gas diffusion-layer-coated catalysts. The electrolytes (20 ml of KOH solution of various concentrations) were circulated through both the anode and cathode chambers. The electrolyte flow was kept at 10 ml min^{-1}. The CO (Linde, 99.99%) flow was kept constant at 50 ml min^{-1} using a mass flow controller.

Electrochemical active surface area measurement. Surface roughness factors for the four catalytic electrodes relative to the polycrystalline Cu foil were estimated from double layer capacitances (C_{dl})[35]. C_{dl} was determined by measuring the geometric current at a potential window at which no Faradaic process occurred as a function of the scan rate of the cyclic voltammetry stripping. For this, cyclic voltammetry was performed in a 1 M KOH electrolyte with an anion exchange membrane. The potential window was between 0.19 V and 0.26 V versus RHE. The scan rates were from 40 mV s^{-1} to 160 mV s^{-1} with an interval of 20 mV s^{-1}. C_{dl} was estimated by plotting the $\triangle j = (j_a - j_c)/2$ at 0.225 V versus RHE (where j_a and j_c are the anodic and cathodic current densities, respectively) against the scan rate. The slope gives the C_{dl} value.

Data availability

The data that support the plots within this paper and other findings of this study are available from the corresponding author upon reasonable request.

Received: 17 June 2018; Accepted: 18 September 2018;
Published online: 29 October 2018

References

1. Lin, S. et al. Covalent organic frameworks comprising cobalt porphyrins for catalytic CO_2 reduction in water. *Science* **349**, 1208–1213 (2015).
2. Asadi, M. et al. Nanostructured transition metal dichalcogenide electrocatalysts for CO_2 reduction in ionic liquid. *Science* **353**, 467–470 (2016).
3. Jiang, K. et al. Metal ion cycling of Cu foil for selective C–C coupling in electrochemical CO_2 reduction. *Nat. Catal.* **1**, 111–119 (2018).
4. Zhuang, T.-T. et al. Steering post-C–C coupling selectivity enables high efficiency electroreduction of carbon dioxide to multi-carbon alcohols. *Nat. Catal.* **1**, 421–428 (2018).
5. Gao, S. et al. Partially oxidized atomic cobalt layers for carbon dioxide electroreduction to liquid fuel. *Nature* **529**, 68–71 (2016).

6. Hahn, C. et al. Engineering Cu surfaces for the electrocatalytic conversion of CO_2: controlling selectivity toward oxygenates and hydrocarbons. *Proc. Natl Acad. Sci. USA* **114**, 5918–5923 (2017).
7. Xiao, H., Goddard, W. A., Cheng, T. & Liu, Y. Cu metal embedded in oxidized matrix catalyst to promote CO_2 activation and CO dimerization for electrochemical reduction of CO_2. *Proc. Natl Acad. Sci. USA* **114**, 6685–6688 (2017).
8. De Luna, P. et al. Catalyst electro-redeposition controls morphology and oxidation state for selective carbon dioxide reduction. *Nat. Catal.* **1**, 103–110 (2018).
9. Schouten, K. J. P., Calle-Vallejo, F. & Koper, M. A step closer to the electrochemical production of liquid fuels. *Angew. Chem. Int. Ed.* **53**, 10858–10860 (2014).
10. Loiudice, A. et al. Tailoring copper nanocrystals towards C2 products in electrochemical CO_2 reduction. *Angew. Chem. Int. Ed.* **55**, 5789–5792 (2016).
11. Ren, D., Wong, N. T., Handoko, A. D., Huang, Y. & Yeo, B. S. Mechanistic insights into the enhanced activity and stability of agglomerated Cu nanocrystals for the electrochemical reduction of carbon dioxide to *n*-propanol. *J. Phys. Chem. Lett.* **7**, 20–24 (2016).
12. Kim, D., Kley, C. S., Li, Y. & Yang, P. Copper nanoparticle ensembles for selective electroreduction of CO_2 to C2–C3 products. *Proc. Natl Acad. Sci. USA* **114**, 10560–10565 (2017).
13. Verma, S., Lu, X., Ma, S., Masel, R. I. & Kenis, P. J. The effect of electrolyte composition on the electroreduction of CO_2 to CO on Ag based gas diffusion electrodes. *Phys. Chem. Chem. Phys.* **18**, 7075–7084 (2016).
14. Jhong, H. R. M. et al. A nitrogen-doped carbon catalyst for electrochemical CO_2 conversion to CO with high selectivity and current density. *ChemSusChem* **10**, 1094–1099 (2017).
15. Kuhl, K. P., Cave, E. R., Abram, D. N. & Jaramillo, T. F. New insights into the electrochemical reduction of carbon dioxide on metallic copper surfaces. *Energy Environ. Sci.* **5**, 7050–7059 (2012).
16. Kortlever, R., Shen, J., Schouten, K. J. P., Calle-Vallejo, F. & Koper, M. T. M. Catalysts and reaction pathways for the electrochemical reduction of carbon dioxide. *J. Phys. Chem. Lett.* **6**, 4073–4082 (2015).
17. Seifitokaldani, A. et al. Hydronium-induced switching between CO_2 electroreduction pathways. *J. Am. Chem. Soc.* **140**, 3833–3837 (2018).
18. Li, C. W., Ciston, J. & Kanan, M. W. Electroreduction of carbon monoxide to liquid fuel on oxide-derived nanocrystalline copper. *Nature* **508**, 504 (2014).
19. Verdaguer-Casadevall, A. et al. Probing the active surface sites for CO reduction on oxide-derived copper electrocatalysts. *J. Am. Chem. Soc.* **137**, 9808–9811 (2015).
20. Xiao, H., Cheng, T. & Goddard, W. A. III Atomistic mechanisms underlying selectivities in C1 and C2 products from electrochemical reduction of CO on Cu(111). *J. Am. Chem. Soc.* **139**, 130–136 (2016).
21. Yang, K. D. et al. Morphology-directed selective production of ethylene or ethane from CO_2 on a Cu mesopore electrode. *Angew. Chem. Int. Ed.* **56**, 796–800 (2017).
22. Zheng, G. et al. Interconnected hollow carbon nanospheres for stable lithium metal anodes. *Nat. Nanotech.* **9**, 618–623 (2014).
23. Li, Z. et al. A sulfur host based on titanium monoxide@carbon hollow spheres for advanced lithium–sulfur batteries. *Nat. Commun.* **7**, 13065 (2016).
24. Wu, H.-L. et al. Formation of pseudomorphic nanocages from Cu_2O nanocrystals through anion exchange reactions. *Science* **351**, 1306–1310 (2016).
25. Kuo, C.-H. & Huang, M. H. Fabrication of truncated rhombic dodecahedral Cu_2O nanocages and nanoframes by particle aggregation and acidic etching. *J. Am. Chem. Soc.* **130**, 12815–12820 (2008).
26. Mistry, H. et al. Highly selective plasma-activated copper catalysts for carbon dioxide reduction to ethylene. *Nat. Commun.* **7**, 12123 (2016).
27. Sen, S., Liu, D. & Palmore, G. T. R. Electrochemical reduction of CO_2 at copper nanofoams. *ACS Catal.* **4**, 3091–3095 (2014).
28. Favaro, M. et al. Subsurface oxide plays a critical role in CO_2 activation by Cu(111) surfaces to form chemisorbed CO_2, the first step in reduction of CO_2. *Proc. Natl Acad. Sci. USA* **114**, 6706–6711 (2017).
29. Rasul, S. et al. A highly selective copper–indium bimetallic electrocatalyst for the electrochemical reduction of aqueous CO_2 to CO. *Angew. Chem. Int. Ed.* **7**, 2146–2150 (2015).
30. Thang Dinh., C. et al. CO_2 electroreduction to ethylene via hydroxide-mediated copper catalysis at an abrupt interface. *Science* **360**, 783–787 (2018).
31. Hori, Y., Takahashi, R., Yoshinami, Y. & Murata, A. Electrochemical reduction of CO at a copper electrode. *J. Phys. Chem. B* **101**, 7075–7081 (1997).
32. Unver, A. & Himmelblau, D. Diffusion coefficients of CO_2, C_2H_4, C_3H_6 and C_4H_8 in water from 6 to 65 °C. *J. Chem. Eng. Data* **9**, 428–431 (1964).
33. Hao, L. & Leaist, D. G. Binary mutual diffusion coefficients of aqueous alcohols. Methanol to 1-heptanol. *J. Chem. Eng. Data* **41**, 210–213 (1996).
34. Cussler, E. L. *Diffusion: Mass Transfer in Fluid Systems* (Cambridge Univ. Press, Cambridge, 2009).
35. Waszczuk, P., Zelenay, P. & Sobkowski, J. Surface interaction of benzoic-acid with a copper electrode. *Electrochim. Acta* **40**, 1717–1721 (1995).

Acknowledgements

This work was supported by the Ontario Research Fund Research-Excellence Program, the Natural Sciences and Engineering Research Council (NSERC) of Canada, the CIFAR Bio-Inspired Solar Energy program and University of Toronto Connaught grant. The authors thank T. P. Wu, Z. Finfrock and L. Ma for technical support at the 9BM beam-line of the Advanced Photon Source (Lemont, IL). This research used resources of the Advanced Photon Source, an Office of Science User Facility operated for the US Department of Energy (DOE) Office of Science by Argonne National Laboratory and was supported by the US DOE under Contract no. DE-AC02-06CH11357, and the Canadian Light Source and its funding partners. S.H.Y. acknowledges funding from the National Natural Science Foundation of China (Grant 21431006) and the Foundation for Innovative Research Groups of the National Natural Science Foundation of China (Grant 21521001). The authors thank X. Wang and A. Seifitokaldani from the University of Toronto for fruitful discussions.

Author Contributions

E.H.S. and D.S. supervised the project. T.-T.Z. designed the structures, carried out the experiments and wrote the paper. Y.P. carried out the FEM simulations. Z.Q.L. and Y.L. helped to synthesize the catalysts and collect the electroreduction performance data. Z.W. helped to do the DFT simulations. C.-S.T. and P.-L.H. helped to characterize the morphology of the catalyst. J.L. performed the X-ray spectroscopy measurements. M.L., A.P. and A.J. carried out the grazing incidence wide-angle X-ray scattering measurements. All the authors discussed the results and assisted during the manuscript preparation.

Competing interests

The authors declare no competing interests.

Additional information

Supplementary information is available for this paper at https://doi.org/10.1038/s41929-018-0168-4.

Reprints and permissions information is available at www.nature.com/reprints.

Correspondence and requests for materials should be addressed to D.S. or E.H.S.

Publisher's note: Springer Nature remains neutral with regard to jurisdictional claims in published maps and institutional affiliations.